Unraveling the Formation Mechanism of the 2D/3D Perovskite Heterostructure for Perovskite Solar Cells Using Multi-Method Characterization

Thomas Campos, Pia Dally, Stéphanie Gbegnon, Alexandre Blaizot, Gaëlle Trippé-Allard, Marion Provost, Muriel Bouttemy, Aurélien Duchatelet, Damien Garrot, Jean Rousset, et al.

▶ To cite this version:

Thomas Campos, Pia Dally, Stéphanie Gbegnon, Alexandre Blaizot, Gaëlle Trippé-Allard, et al.. Unraveling the Formation Mechanism of the 2D/3D Perovskite Heterostructure for Perovskite Solar Cells Using Multi-Method Characterization. Journal of Physical Chemistry C, 2022, 126 (31), pp.13527-13538. 10.1021/acs.jpcc.2c04957 . hal-03779926

HAL Id: hal-03779926
https://hal.science/hal-03779926v1

Submitted on 15 Jul 2024

Unraveling the Formation Mechanism of 2D/3D Perovskite Heterostructure for Perovskite Solar Cells using Multi-Method Characterization

Thomas Campos *,1,2, *Pia Dally* 2,5, *Stéphanie Gbegnon* 2, *Alexandre Blaizot* 2, *Gaëlle Trippé-Allard* 1, *Marion Provost* 2, *Muriel Bouttemy* 5, *Aurélien Duchatelet* 2,3, *Damien Garrot* 4, *Jean Rousset* 2,3, *Emmanuelle Deleporte* 1

[1] Lumière, Matière et Interfaces (LuMIn) Laboratory, Université Paris-Saclay, ENS Paris-Saclay, CNRS, CentraleSupelec, 91190 Gif-sur-Yvette, France * thomas.campos@ens-paris-saclay.fr

[2] Institut Photovoltaïque d'Ile-de-France (IPVF), 18 Boulevard Thomas Gobert, 91120 Palaiseau, France

[3] EDF R&D, Boulevard Gaspard Monge, 91120 Palaiseau, France

[4] Groupe d'Etudes de la Matière Condensée (GEMAC), Université Versailles Saint-Quentin en Yvelines, CNRS, 45 avenue des Etats-Unis, 78000 Versailles, France

[5] Institut Lavoisier de Versailles (ILV), Université de Versailles Saint-Quentin-en-Yvelines, Université Paris-Saclay, CNRS, UMR 8180, 45 avenue des États-Unis, 78035 Versailles, France

Abstract

The formation of a two-dimensional (2D) three-dimensional (3D) perovskite heterostructure has lately proved to be a promising way to improve the interface between the perovskite and electron/hole transport layers (ETL/HTL) in perovskite solar cells (PSCs), which is crucial for better device efficiency and stability. Herein, a spacer cation, 4-fluorophenethylammonium iodide (4-FPEAI), in isopropyl alcohol (IPA) was used to form a thin 2D perovskite layer on top of a 3D triple-cation perovskite, by a spin-coating deposition process. Therefore, a significant improvement in the device's open-circuit voltage is obtained, leading to an enhanced power conversion efficiency (PCE). The formation mechanism of the 2D perovskite layer was studied by analyzing the structural, chemical, and optoelectronic properties of the layer while varying several synthesis parameters. We reveal the presence of bromide inside the 2D phase and conclude with the existence of a concomitant formation mechanism besides the most commonly described one involving the lead iodide (PbI_2) excess contained in the 3D bulk. Therefore, we demonstrate how the stoichiometry of the 2D perovskite is affected by the chemical composition of the 3D layer underneath. This work brings new insight into the synthesis mechanisms of 3D/2D perovskite heterostructures, which could help to optimize their fabrication processes and develop new efficient and functional 3D/2D structures.

1. Introduction

Perovskite solar cells (PSCs), using hybrid metal halide three-dimensional (3D) perovskites as the active layer, have known a tremendous performance increase over the last decade.[1,2] Their power conversion efficiency (PCE) has risen from 3.8% in 2009 to 25.7% nowadays as a single cell, closing the gap with silicon technology.[3–5] This rapid development arises from the significant attention paid to 3D perovskites, justified by many advantages, such as their excellent optoelectronic properties, making them a good candidate for silicon tandem cells, or their low-temperature chemical solution processability.[1,2,4,6–11] Many improvements were made toward the intrinsic and extrinsic instabilities of the material when exposed to light, temperature, oxygen, and moisture.[12] However, stability is still one of the remaining issues to solve for the commercialization of the perovskite technology.[13,14]

In order to enhance the stability of perovskite-based solar cells, numerous approaches have been used, such as tuning the 3D perovskite absorber composition or optimizing the device architecture with the modification of electron/hole transport layers (ETL/HTL).[15–20] Particular attention has been given to the interfaces, specifically to surface passivation, given the crucial role of the interfaces in improving device efficiency and stability.[17,21,22] For this purpose, combining 2D perovskites with 3D perovskites, creating a so-called 2D/3D heterostructure on the surface of the 3D perovskite, is a promising approach.[17,23–25]

Two-dimensional (2D) layered Ruddlesden-Popper (RP) perovskites appeared to be an interesting alternative to 3D perovskites in PSCs, thanks to their better stability.[23,26] These perovskite materials are obtained using a bigger organic spacer cation that organizes the structure into a stacking of inorganic BX_6^{4-} (usually PbI_6^{4-}) and organic spacer monolayers. The chemical formula of 2D RP perovskites is defined as $R_2A_{n-1}B_nX_{3n+1}$, where A, B, and X respectively define:

monovalent organic cations (i.e., methylammonium MA^+); divalent metal cations (i.e., lead Pb^{2+}); and halide anions (i.e., iodine I^-).[27] R is a large aromatic or aliphatic alkylammonium spacer cation (i.e., phenylethylammonium PEA^+). The n factor is the number of consecutive inorganic PbI_6^{4-} layers between two R-based organic layers and sets the nature of the material: a value of one gives a strict 2D perovskite of R_2BX_4 formula, while an infinite value leads to a strict 3D perovskite of formula ABX_3.[28,29] Several elements limit the use of 2D perovskites for solar cells, such as their much wider bandgap than 3D perovskites (>2 eV), suboptimal for single-junction and tandem solar cells.[30] Also, because of their layered structure, they present higher exciton binding energies, and anisotropic charge transport properties - with a high conductivity along the inorganic layers and poor conductivity across the stack due to the insulating nature of the organic layers - making the crystalline orientation a critical aspect for the performances of 2D PSCs.[29,30]

Thanks to the chemical versatility of 2D perovskites, a considerable amount of spacers can be used, such as aromatic cations, including phenethylammonium (PEA^+) or benzylammonium (BZA^+), or alkyl chains such as n-butylammonium or n-octylammonium ($n\text{-}BA^+$ or $n\text{-}OA^+$).[24,25,31,32] To form a 2D/3D heterostructure, the spacer cation is combined with a halide anion, and it is also possible to substitute this halide, like phenethylammonium iodide (PEAI) or bromide (PEABr).[33,34] Each combination has specific optoelectronic properties and thus, could be chosen according to the 3D perovskite used.[35]

Remarkable achievements have been made on PCE and stability improvements of 2D/3D heterostructures compared to pristine 3D material.[17,36–38] Using new 2D cations and innovative architectures, much knowledge was acquired on the 2D/3D structure and how it improves device performances thanks to properties like surface passivation, reduction of non-radiative recombination, or inhibition of ionic migration.[25,37,39–42] Despite this significant progress, understanding the phenomena driving the formation of the 2D/3D interface remains a crucial challenge for the development of this complex structure and to improve even further device optimization.[25,38,43]

Here, we investigate the formation mechanism of a 2D/3D heterostructure on the common and efficient $(Cs,MA,FA)Pb(I,Br)_3$ triple-cation perovskite surface by an isopropanol (IPA) solution processing containing a halide salt, 4-fluorophenylethylammonium iodide (4-FPEAI). The use of 4-FPEAI has a double purpose, as fluorine improves the hydrophobicity of the 2D cation and changes its dipole moment, modifying the electronic properties of the layer compared to non-fluorinated PEAI cation. As a result, device efficiency and stability are further increased.[44,45] In the present study, fluorine is used as a probe element for X-Ray photoelectron spectroscopy (XPS) chemical characterization to track the 2D perovskite layer formation. A systemic study of the 2D layer formation as a function of the synthesis parameters is performed using structural, chemical, and optoelectronic characterization techniques. This work highlights the importance of the 2D cation concentration and its impact on the physical properties of the 2D perovskite layer formed. It also reveals the presence of bromine in the 2D phase, affecting its optical properties. We suggest that the presence of bromine in the 2D layer is due to two concomitant formation mechanisms: the reaction between the 4-FPEAI and the lead iodide (PbI_2) excess in the 3D perovskite, competing with a cation exchange between 4-FPEAI and the 3D perovskite to form a 2D perovskite with a significant bromine amount.

2. Experimental section

Materials: FTO substrates were purchased from Solems. Titanium dioxide (TiO_2) paste 30NR-D, methylammonium iodide (MAI, > 99.99%), methylammonium bromide (MABr, > 99.99%), formamidinium iodide (FAI, > 99.99%), and FK 209 Co(III) TFSI Salt were all purchased from Greatcell Solar Materials. Lead bromide ($PbBr_2$, ultra dry 99.999%) and lead iodide (PbI_2, ultra dry 99.999%) were purchased from Alfa Aesar. Cesium iodide (CsI, 99.999%), N,N-dimethylformamide (DMF, anhydrous 99.8%), dimethylsulfoxide (DMSO, ≥ 99.7%), chlorobenzene (CB, anhydrous 99.8%), isopropanol (IPA, anhydrous 99.5%), bis(trifluoromethane)sulfonimide lithium salt (Li-TFSI, 99.95%), and 4-tert-butylpyridine (t-BP, 98%), were all purchased from Sigma-Aldrich. 2,2’,7,7’-tetrakis [N,N-di (4-methoxyphenyl)amino]-9,9’- spirobifluorene (Spiro-OMeTAD) was purchased from Borun New Materials. All materials were used without further purification.

Synthesis of 4-fluorophenylethylammonium iodide (4-FPEAI) salts: 4-fluorophenylethylamine (5 mL, 38.1 mmol) in ethanol (20 mL) was added drop by drop to a solution in ethanol (50 mL) of hydriodic acid (57 %, 5.3 mL, 1.05 eq.) and hydrophosphoric acid (0.5 mL) cooled to 0°C. The solution was then stirred at room temperature for 1 hour before removing the solvent in vacuo. The crude was purified by recrystallization in ethanol, forming 4-FPEAI white crystals with a 69 % yield (7.0 g).

Sample fabrication: FTO-coated glass substrates ($2x2cm^2$) were cleaned with sequential sonication in detergent (30 min), acetone (15 min), and isopropanol (15 min) baths at 50°C. Following clear airflow drying, the cleaned substrates were treated with UV-Ozone for 15 min. A compact-TiO_2 electron transport layer (ETL) was made thanks to atomic layer deposition (ALD). After that, a mesoporous-TiO_2 layer was deposited in an ambient atmosphere with the spin-coating of a TiO_2 paste solution in ethanol (1:7 weight ratio) at a speed of 4000rpm for 30 s, and annealed on a hot plate for 45 min with several temperature steps, up to 500°C. A specific tin chloride ($SnCl_4$) treatment was specifically applied on the mesoporous TiO_2 layer for stability measurements. The Glass/FTO/TiO_2 substrates were treated with UV-Ozone for 30 min before being introduced in a glovebox for perovskite deposition.

The triple-cation perovskite solution was prepared by preparing a solution of CsI (1.5mmol) in 1mL of DMSO. This solution was stirred overnight at room temperature before being used. Another solution was prepared by dissolving MABr (0.2mmol), $PbBr_2$ (0.2mmol), FAI (1mmol) and PbI_2 (1.1mmol) in 1mL of a DMF and DMSO mix (4 :1 volume ratio). For the full iodide perovskite, MABr and $PbBr_2$ were replaced with MAI and PbI_2. For PbI_2 excess variation, the PbI_2 amount was reduced to 1mmol for the "lack of PbI_2" sample. This solution was stirred for 2 h at room temperature. After that, 1mL of this solution was mixed with 42 µL of the CsI solution and stirred for another 15 minutes before deposition. To prepare 3D perovskite films, the perovskite solution was spin-coated on top of the TiO_2 layer at 2000 rpm for 12 s. A second consecutive step of 30 s at 6000 rpm was used to deposit 100 µL of chlorobenzene 12 s before the end of the rotation. The intermediate films were then annealed on a hot plate at 100°C for 30 min for perovskite film formation. For the 4-FPEAI treated samples, the 2D cation was dissolved in IPA with several concentrations (2.5, 5, and 10mg.mL^{-1}) and stirred for 2 h at room temperature. 100 µL of the 4-FPEAI solutions were then spin-coated onto the 3D perovskite at 4000 rpm for 30 s and annealed at 100°C for 5 min. Samples for characterization were left as half-cells after either 3D perovskite or 4-FPEAI solution deposition for pristine and 4-FPEAI treated samples. A spiro-OMeTAD solution was prepared for solar cell devices by dissolving 110 mg of spiro-OMeTAD in 1 mL of chlorobenzene and doping it with 17 µL of FK-209, 25 µL of LiTFSI, and 45 µL of t-BP. 35 µL of this solution was spin-coated onto the perovskite at 3000 rpm for 30 seconds. Finally, a thermal evaporation process deposited a 100 nm thick gold electrode on top of the cell.

Pure 2D perovskite samples were made on ITO-coated glass substrates. These substrates (2x2 cm²) were cleaned with the same sonication process as FTO-glass substrates and treated with UV-Ozone for 30 minutes before glovebox introduction. A 2D precursor solution was realized by mixing 4-FPEAI cation and PbI_2 with a 2:1 molar ratio. This mix was dissolved in a DMF and DMSO mix (4:1 volume ratio) with a 10% weight concentration and stirred at room temperature for 3 h. For the 2D perovskite formation, 100 µL of the precursor solution was spin-coated in the ITO substrate at 2000 rpm for 30 s. 100 µL of toluene was then deposited during a second iteration of the same spin-coating program. The perovskite was crystallized with hot plate annealing of 100°C for 1 min.

Characterizations: For crystal structure characterization of the perovskite thin film, a Panalytical XRD analyzer was used (Cu Kα1α2 radiation, λ ¼ 1.5418 Å). SEM images were made using a Zeiss Merlin VP Compact field emission scanning electron microscope to observe the morphology of the perovskite film. AFM images (10x10 µm²) were acquired with an Agilent 5600 LS atomic force microscope, using an ACL probe from AppNano in tapping mode under ambient air. Sq and Sa roughness values were extracted from images thanks to Gwyddion software. The optical microscopy Sq and Sa roughness values were obtained with an Olympus LEXT OLS5100 confocal microscope and were measured from a 3D acquisition of the sample surface (129x129 μm^2 area).

PL spectra were obtained with a micro-photoluminescence setup. The sample was illuminated through a Nikon microscope objective with a 40x magnification and a 0.6 numerical aperture with a 405 nm impulsionnal PDL 800-D PicoQuant laser diode with an 80 MHz frequency. The sample luminescence went through the same objective and was separated from the excitation beam with a beam splitter and LP filter. It was finally sent through a Spectrapro 2500i spectrometer and collected by a PyLoN® CCD camera, both controlled with the LightField software from Princeton Instruments.

For XPS surface chemical analysis, freshly synthesized perovskite samples were transferred to the XPS spectrometer in the dark and under inert atmosphere conditions to ensure the reliability of the analysis. The measurements were carried out with a Thermo Electron K-Alpha+ spectrometer equipped with a monochromated Al-Kα X-Ray source for excitation at 1486.6 eV in an X-ray spot size of 400 µm. Calibration of the spectrometer was done using Cu and Au samples following the ASTM-E-902-94 protocol. The constant analyzer energy (CAE) mode was used to acquire high energy resolution spectra with a pass energy of 20 eV and an energy step size of 100 meV. Thermo Fisher scientific Avantage© data system was used for data treatment and peak fitting. A set of 10 analyses points was randomly positioned on several 2x2 cm² samples to certify the reliability of the information collected. An optimized analysis procedure[46] was employed to ensure no X-ray damage or UHV degradation occurred.

For device current density-voltage (J-V) characterization, a 3 A xenon lamp simulator from Newport (300 W) with AM 1.5G solar spectrum filter and light intensity of 100 $mW.cm^{-2}$ was used, with samples remaining in ambient conditions. The active area of the devices was framed with a 0.09 cm² metal mask. After a 30 s exposition to the light source for light soaking, the J–V curves were scanned in both forward and reverse directions with a computer-controlled Keithley, within a -0.2 to 1.2 V range, at a scanning speed of 20 $mV.s^{-1}$.

3. Results and Discussion

3.1. Effect of 4-FPEAI concentration on the 2D layer physical properties

This work is based on a comparative study between a $(4\text{-FPEA})_2PbI_4$ pure 2D perovskite (called pure 2D), a triple-cation $Cs_{0.05}(MA_{0.17}FA_{0.83})_{0.95}Pb(I_{0.83}Br_{0.17})_3$ 3D perovskite with a 2.0% PbI_2 excess (named pristine), and 2D/3D perovskite heterostructures. The 2D/3D structure is obtained by treating the 3D perovskite with a solution of 4-FPEAI dissolved in IPA with three concentrations: 2.5, 5, and 10 $mg.mL^{-1}$ (later named 2.5mg.mL^{-1}, 5mg.mL^{-1}, and 10mg.mL^{-1}). This process is illustrated in Supplementary Figure S1. All samples were studied with the following half-cell architecture: glass/FTO/c-TiO_2/m-TiO_2/Perovskite. Synthesis details of pure 2D and pristine 3D are shown in the Experimental section.

The focus of this study is to analyze the influence of the 4-FPEAI solution concentration on the formation mechanism of the 2D perovskite phase. In the first place, we fabricated photovoltaic devices using 2D/3D structures to validate the fabrication process (NIP device architecture in Supplementary Figure S1). We determined the optimum 4-FPEAI solution concentration for device efficiency in Supplementary Figure S2. Solar cells based on 2.5mg.mL^{-1} treated perovskite displayed the best results. Higher concentrations were detrimental to cell performances due to a quick loss of short-circuit current density (J_{SC}) and fill factor (FF) as the thickness, and thus the resistivity of the 2D layer, increased. The best current-voltage characteristic and photovoltaic parameters for both pristine and 2.5mg.mL^{-1} cells are displayed in Figure 1a. The effect of 4-FPEAI treatment on the device stability was assessed with maximum power point tracking (MPPT) of encapsulated devices under a continuous 1-sun illumination (without UV) with controlled temperature. The results (Figure 1b) show an important improvement of the stability with the 2D perovskite addition, with 70% of the initial PCE remaining after 110 hours under illumination, compared to 32% for the pristine sample. Statistics on the photovoltaic parameters of eight cells are presented in Figures 1c-f. These results report a significant average increase of 40±14 mV in open-circuit voltage (V_{OC}) with 4-FPEAI treatment, consistent with the literature indication of surface passivation by the 2D perovskite.[25,34,38] Short-circuit current density (J_{SC}) and fill factor (FF) remain statistically similar to the pristine samples. Thus, the 4-FPEAI treatment leads to an increase of 0.8±0.9 % in power conversion efficiency (PCE) compared to pristine devices. These results validate our 4-FPEAI treatment process and encourage us to develop it further to increase the efficiency of our solar cell devices. Further optimizations of the process would be required to reach the same level of performance reached in the literature with this widely used triple-cation composition.[23,25]

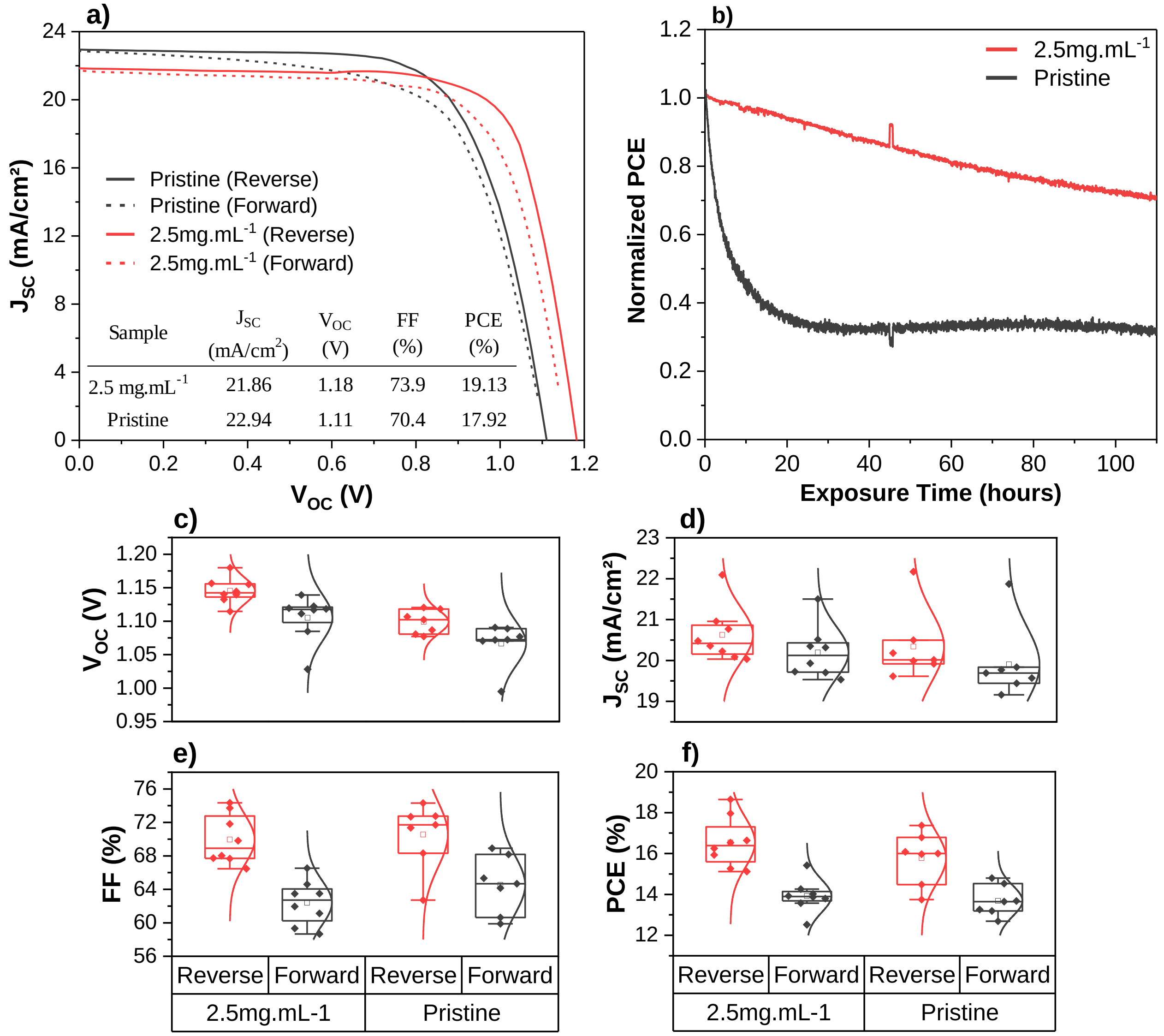

Figure 1. a) Best J-V characteristic of the PSCs using pristine or 2.5mg.mL^{-1} treated perovskite. b) MPPT of pristine and 2.5mg.mL^{-1} treated cell under continuous 1-sun illumination (without UV) c-f) Photovoltaic parameters (V_{OC}, J_{SC}, FF, and PCE) statistics between pristine and 2.5mg.mL^{-1} treated perovskite on eight devices for reverse and forward measurements after fabrication.

X-ray diffraction (XRD) was carried out to assess the structural properties of the 2D layer for 4-FPEAI treated samples. A pure 2D perovskite and a pristine 3D perovskite reference samples were first compared to a 10mg.mL^{-1} sample as displayed in Figure 2a. In the pure 2D pattern, peaks located at 5.4, 10.8, 16.3, 21.7, 27.2, and 32.8° correspond to the (002), (004), (006), (008), (0010), and (0012) plans of the 2D phase. 3D perovskite (001), (011), (111), (002), and (012) plans are respectively attributed to the characteristic peaks at 14.1, 20, 24.5, 28.4, and 31.8°. The peak centered at 12.7° is attributed to PbI_2, given the 2.0% PbI_2 excess introduced in the perovskite precursor solution.[47] The comparison in Supplementary Figure S3 between Bragg-Brentano and grazing incidence XRD spectra (respectively scanning the whole layer and only the first few hundred nanometers) of a pristine sample shows that this PbI_2 peak is mainly localized on the 3D perovskite surface.

The 10mg.mL^{-1} sample displays all peaks from the 3D perovskite, with the addition of 5.4 and 27.2° peaks from the 2D phase, showing that the deposition method succeeds in forming a 2D perovskite layer on the 3D bulk. However, the intensity of the peaks from the 2D phase remains low compared to those of the 3D phase, indicating a presumed low thickness.

Figure 2b shows the evolution of the XRD pattern as a function of the 4-FPEAI solution concentration, zoomed on the angle range where the first 2D and 3D peaks appear. While increasing the concentration of the 4-FPEAI treatment, two behaviors are induced: the peak at 5.4° related to the 2D phase appears, and its intensity increases, and secondly, the intensity of the PbI_2 peak at 12.7° progressively decreases. These observations underline the reaction between the 2D cation, here 4-FPEAI, and the surface PbI_2 excess of the 3D phase, to form a pure 2D perovskite:

$$2(\text{4-FPEAI}) + PbI_2 \rightarrow (\text{4-FPEA})_2PbI_4 \qquad \text{Eq. 1}$$

Thus, as 4-FPEAI concentration increases, more PbI_2 is consumed for the reaction, leading to the XRD PbI_2 peak disappearance for the highest 4-FPEAI solution concentration. This result is in agreement with the literature.[38,48]

To investigate the evolution of film morphology and coverage with 4-FPEAI treatment, scanning electron microscopy (SEM) and atomic force microscopy (AFM) images of the surface of pristine and 4-FPEAI treated samples were realized and are presented in Figures 2c-e and Supplementary Figure S4a-c. Only images of the limit 2.5 and 10 mg.mL^{-1} concentrations, presenting the most visible surface evolution, are shown here. The pristine perovskite shows the classical morphology of a 3D perovskite layer composed of crystalline grains of about 300 nm (Figure 2c). For the 2.5mg.mL^{-1} sample, depositing a weakly concentrated solution visually seems to drive the formation of a thin homogeneous layer that smooths the space between grains and levels the surface (Figure 2d). However, 3D perovskite grains are still visible underneath, indicating the low 2D layer thickness. This observation is confirmed by AFM images (Supplementary Figures S4a and S4b), as the topographic amplitude shrinks from 160 nm for the pristine sample to 99 nm for the 2.5mg.mL^{-1} sample. For the 10mg.mL^{-1} highest concentration, both SEM and AFM (Figure 2e and Supplementary Figure S4c) show less visible 3D perovskite grains, suggesting the 2D perovskite thickness has increased. The cross-section SEM image in Figures 2f-g supports this observation, evidencing the formation of many 2D perovskite grains on the 3D layer, a few tens of nanometers wide, significantly covering the surface. By correlating this image with the size of the small grains visible on the surface of the 10mg.mL^{-1} sample in Figure 2e, we estimate the 2D layer thickness for this concentration not to exceed 30nm. Hence, these results confirm the formation of a 2D layer on the 3D perovskite bulk, changing the surface morphology according to the 4-FPEAI solution concentration.

Supplementary Figures S5a-d displays the statistical distribution of AFM surface roughness measurements, performed on pristine and all 4-FPEAI treated samples, correlated with roughness measurements performed with a confocal microscope. This study attests to the representativeness of morphological analyses and confirms that a weakly concentrated 4-FPEAI solution improves the surface smoothness due to the 2D top layer formation. As a result, the average Sq roughness of pristine samples decreases from 25.69 nm to 17.95 nm with 2.5mg.mL^{-1} 4-FPEAI treatment.

Increasing the concentration to 5 mg.mL^{-1} further decreases the roughness to 17.05 nm. However, for the 10 mg.mL^{-1} concentration, the roughness worsens up to a value of 22.20 nm, revealing that forming a significantly thicker 2D layer reduces the smoothness of the surface, in line with the morphological changes (visible sub micrometer grains inhomogeneous distribution).

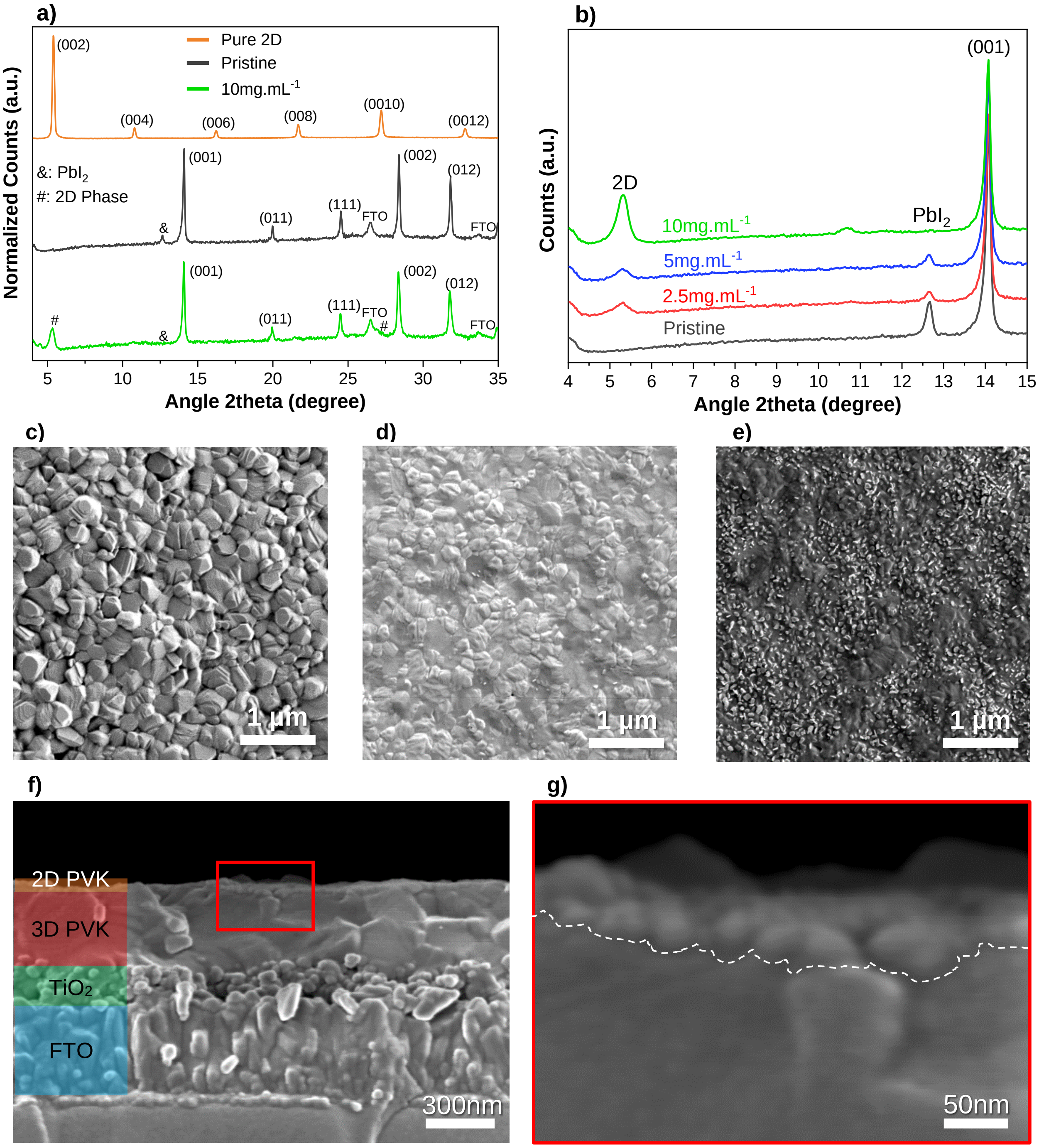

Figure 2. a) Bragg XRD diffractogram of a pure 2D perovskite, a pristine 3D perovskite, and a 10mg.mL^{-1} sample. b) Diffractogram of pristine and 4-FPEAI treated samples zoomed on the 2D phase peak. SEM images of the surface of c) pristine, d) 2.5mg.mL^{-1}, and e) 10mg.mL^{-1} samples. f) Cross-section SEM image of a 10mg.mL^{-1} sample, g) zoomed on the 2D perovskite layer.

The optical properties of the 2D/3D structure were analyzed through photoluminescence (PL) measurements performed on pristine and the three 4-FPEAI treated samples. Figure 3a shows the PL intensity for pristine and the three 4-FPEAI treated samples normalized on the 3D perovskite emission. The 3D perovskite peak is located around 760nm and remains unchanged regardless of the 4-FPEAI solution concentration, confirming that the solutions employed do not affect the emission properties and thus, do not damage the 3D perovskite. On the other hand, adding the 2D cation leads to the emergence of two new emission peaks around 510 and 552 nm. Increasing the 4-FPEAI solution concentration enhances the intensity of these peaks, especially for the first one, relatively to the 3D peak intensity. Thus, we could reasonably assume that these peaks correspond to the excitonic transition of n=1 and n=2 RP phases of the $(4\text{-FPEA})_2(\text{MA,FA,Cs})_{n-1}\text{Pb}_n\text{I}_{3n+1}$ 2D perovskite formed by the 4-FPEAI treatment, with a predominance for the n=1 phase.[49]

Figure 3b compares the PL emission of a pure 2D perovskite and the emission from the 2D layer of a 10 mg.mL^{-1} sample. For the pure 2D perovskite, the PL is centered on 525 nm (2.36 eV), consistently with literature data published on iodide 2D perovskites.[49] In comparison, for the 2D perovskite formed on top of a 3D bulk, the PL is centered on 510 nm (2.43 eV), and the emission peak appears broader. The cause of this behavior could be the presence of bromine within the 3D perovskite, which would affect the 2D perovskite composition and lead to a significant amount of bromine in the layer.[50,51] Thus, the excitonic optical transition of the n=1 2D phase, expected at 2.36 eV with only iodine, would be increased to around 2.43 eV as switching from iodine to bromine increases the perovskites' excitonic transition energy, and its PL signal would get broader due to the presence of a halide mixture.[51]

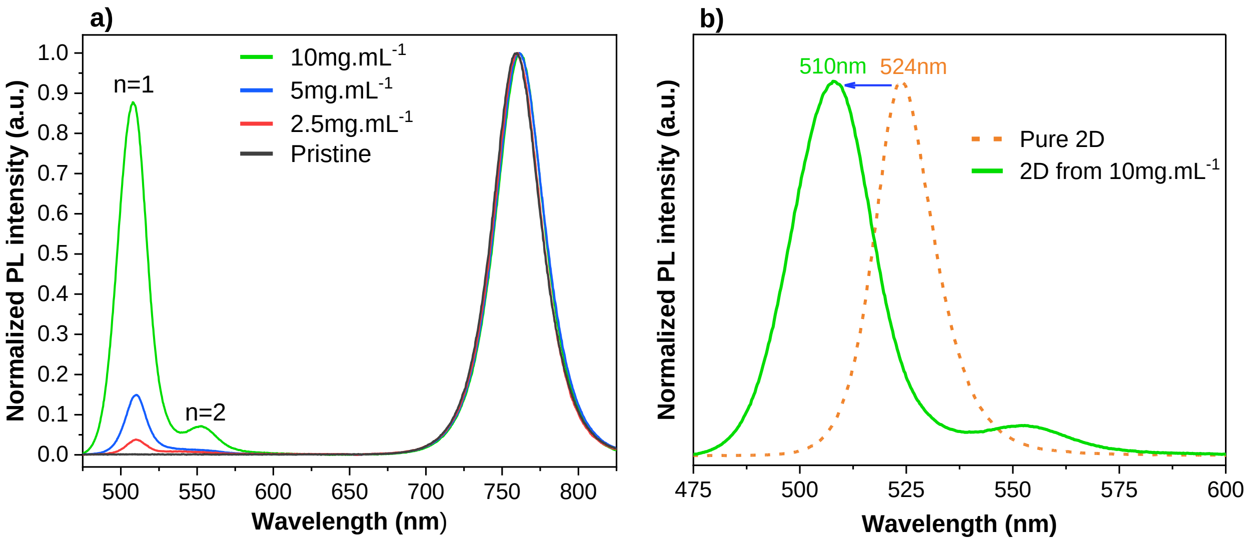

Figure 3. a) Photoluminescence spectra of pristine 3D and 4-FPEAI treated samples with all three concentrations (2.5, 5, and 10mg.mL^{-1}). b) PL spectra comparison between a pure 2D perovskite and the 2D phase formed on top of a 3D layer (for highest concentration 10mg.mL^{-1})

Complementary XPS surface analyses were performed on all 4-FPEAI treated samples to assess the surface chemical modifications that were consecutive to the 2D process for every concentration. For such thin 2D overlayers (ultimate thickness around 30 nm for the highest concentration, close to the 10 nm depth probed with XPS), the main challenge was discriminating the spectral contributions from the superimposed 2D and 3D layers. Indeed, many identical elements constitute both, such as carbon, nitrogen, lead, and iodine, with the only notable exceptions being fluorine for the 2D, and bromine and cesium for the 3D perovskite. Thus, the presence of fluorine is direct evidence of the presence of the 2D layer, while bromine and cesium act as indications in a first approximation of the 3D layer underneath. At first, XPS surface analysis was carried out on the pristine 3D perovskite and the pure 2D perovskite to perform a precise quantification on the separated layers, which will serve as a point of comparison for the 4-FPEAI treated samples.

The XPS high-resolution spectra of F 1s, N 1s, Br 3d, and Cs 3d measured on top of the 4-FPEAI treated samples for each concentration are presented in Figures 4a-d. From a qualitative point of view, F 1s spectra, the characteristic signature of the 2D perovskite (related to the C – F contribution), show an intensity increase while increasing the concentration of the 4-FPEAI solution. This result evidences the 2D layer presence for all concentrations studied. Subsequently, N 1s spectra show a progressive decrease of the signal originating from the imidine bond in FA^+ (400.9 ± 0.2 eV) while increasing the 4-FPEAI concentration, which disappears for the highest $10 mg.mL^{-1}$ concentration. The C – N bond originating from MA^+ contribution in the 3D perovskite and the C – N bond of the 2D molecule have very close binding energies (402.4 ± 0.2 eV), which explains the increase of the peak at 402.4 eV for higher 4-FPEAI concentrations, most probably attributed to the 2D layer. Correspondingly, the Cs $3d_{5/2}$ and Cs $3d_{3/2}$ peaks, respectively positioned at 725.0 and 739.1 eV and attributed to the 3D layer below, also decrease while increasing the 4-FPEAI concentration. Previous SEM and AFM images (Figures 2d-e and Supplementary Figure S4) showed the good coverage and homogeneity of the 2D layer formed. Thus, we conclude that XPS signals observed for $2.5 mg.mL^{-1}$ samples originate from the 2D layer and the 3D perovskite underneath because of the low 2D layer thickness. By increasing the 4-FPEAI concentration, the 2D overlayer gets thicker and progressively masks the 3D layer signal, agreeing with our previous correlations between 4-FPEAI concentration and 2D layer thickness. Surprisingly, the Br 3d spectra, contrarily to Cs 3d, show insignificant intensity change for all studied concentrations. This raises a question about the relation between bromine depth redistribution and its role in the formation mechanism of the 2D perovskite layer.

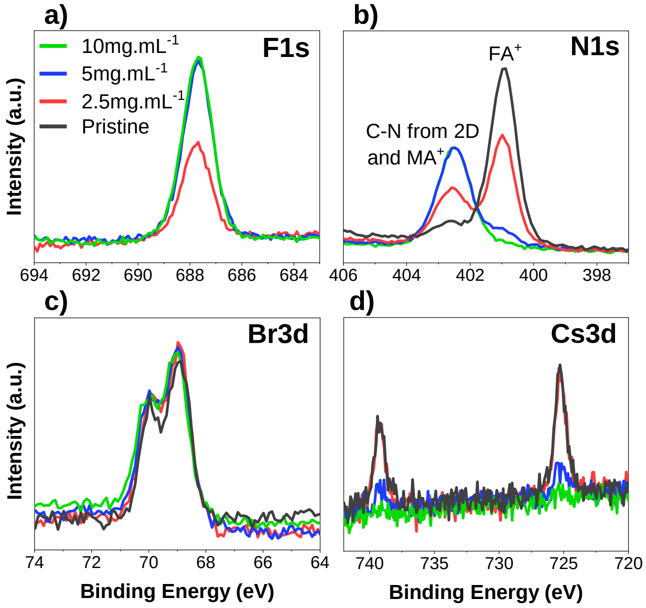

Figure 4. XPS high-resolution spectra of a) F 1s, b) N 1s, c) Br 3d, and d) Cs 3d of pristine and 4-FPEAI treated samples (2.5, 5, and 10 mg.mL^{-1}).

The atomic percentages of every chemical element for the three studied concentrations are gathered in Table 1. The comparison between pristine and 2.5mg.mL^{-1} samples shows a very similar surface composition, suggesting a few nanometers thick 2D layer for this concentration, since the depth probed with the present XPS technique is about 10th of nm. When the concentration increases, the surface stoichiometry of 4-FPEAI treated samples gets closer to the one measured for a pure 2D perovskite, being nearly identical at 10mg.mL^{-1}, in agreement with the SEM thickness measurement of 30 nm for the 2D layer. The amount of bromine on the material's surface remains significantly high regardless of 4-FPEAI concentration, hence, regardless of the 2D layer thickness, emphasizing the role of bromine in the formation of the 2D phase.

	Pristine 3D	2.5mg.mL^{-1}	5mg.mL^{-1}	10mg.mL^{-1}	Pure 2D
C1s	31.6 ± 3.5	46.7 ± 1.2	60.0 ± 0.6	62.6 ± 0.4	62.3 ± 0.7
I3d$_{5/2}$	31.5 ± 2.2	21.3 ± 0.5	14.1 ± 0.5	13.0 ± 0.5	16.3 ± 0.4
N1s	18.2 ± 1.1	13.3 ± 0.3	8.8 ± 0.2	7.9 ± 0.3	7.7 ± 0.2
Pb4f$_{7/2}$	9.4 ± 0.6	6.3 ± 0.2	3.8 ± 0.1	3.4 ± 0.1	3.0 ± 0.1
O1s^{+}	4.5 ± 1.2	1.9 ± 0.2	1.4 ± 0.6	1.4 ± 1.0	1.6 ± 0.9
F1s*	-	5.5 ± 0.2	8.0 ± 0.4	8.3 ± 0.6	8.6 ± 0.2
Cs3d$_{5/2}$$^{\#}$	0.6 ± 0.0	0.4 ± 0.0	0.1 ± 0.0	0.1 ± 0.0	-
Br3d$^{\#}$	5.2 ± 0.3	4.7 ± 0.1	3.8 ± 0.1	3.4 ± 0.1	-

*only in 4-FPEAI, $^{\#}$only in 3D perovskite, $^{+}$ambient carbonaceous contamination

Table 1. XPS atomic percentages of the surface of a pristine 3D perovskite, a pure 2D perovskite, and 4-FPEAI treated samples for all concentrations studied.

3.2. Halide variation in 3D perovskite composition

To get an insight into bromine's role in the formation mechanism and optical properties of the 2D layer, a 5 mg.mL^{-1} 4-FPEAI solution was deposited onto two different 3D perovskites: the one already used in this work (called pristine) and a second perovskite (named full iodide), for which bromine was substituted with iodine, leading to the stoichiometry $Cs_{0.05}(MA_{0.17}FA_{0.83})_{0.95}PbI_3$.

Figure 5 compares the photoluminescence of pristine and full iodide 3D perovskites with 4-FPEAI treatment. The 3D phase emission moves from 760 nm for the pristine sample to almost 800 nm for the full iodide composition, supporting that bromine's removal decreased the 3D perovskite bandgap. The 2D perovskite formed on the pristine 3D shows a main n=1 excitonic peak at 510 nm, with a small contribution from an n=2 phase at 550 nm. When deposited on the full iodide perovskite, the PL intensity of the n=1 and n=2 phases increases, and an insignificant signal appears, expected to come from an n=3 phase. This brighter luminescence could indicate a better formation or improved emission properties of the 2D layer when using only iodine in both the 2D and the 3D compositions instead of an iodine and bromine mix. The n=1 and n=2 2D phases wavelengths red-shifted to 521 and 569 nm when deposited on the full iodide 3D, much closer to the values expected for the excitonic transitions this material (525 nm for n=1). However, a slight difference remains between the emission of the n=1 2D phase on the full iodide 3D and the emission of a pure 2D perovskite (521 nm vs. 525 nm). This difference could be explained by the 3D bulk presence underneath, which would modify the dielectric environment of the PbI_6^{2-} inorganic layer and so the energy of its excitonic transitions (taking into account that the dielectric confinement brings an important contribution to the value of the 2D perovskite exciton binding energy), or by the small thickness of the 2D layer, involving specific constraints modifying the bandgap.[52,53] Nevertheless, this study underlines that bromine from the 3D perovskite is the main reason for the 2D phase PL blue shift, as bromine is also present in the 2D layer composition.

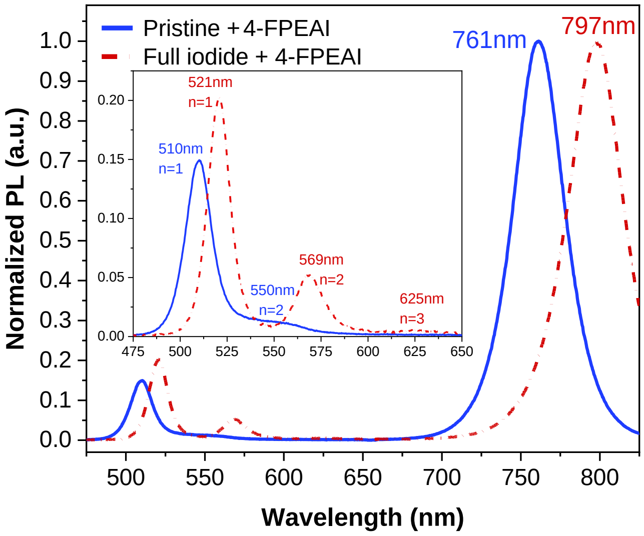

Figure 5. PL of pristine and full iodide 3D perovskites with 4-FPEAI treatment.

To sum up, the 4-FPEAI solution concentration is a key parameter to affect the thickness of the 2D perovskite layer formed, and we demonstrated that this 2D phase contains an iodine and bromine halide mix, shifting the excitonic transitions of the 2D phase towards higher energies. The bromine/iodine ratio, calculated from data presented in Table 1, seems much higher in the 2D phase of the 10mg.mL^{-1} sample (3.4/13) than in the pristine 3D (5.2/31.5). A new question arises from these observations: what mechanism causes the presence of bromine in the 2D layer?

3.3. Expected mechanism and PbI_2 excess variation

As previously detailed, the literature consensus for the formation of the 2D layer is the 4-FPEAI cation reaction with local PbI_2 excess on the 3D perovskite surface following eq. 1, and we confirmed this mechanism earlier in this work through XRD measurements shown in Figures 2a-b. However, this mechanism alone cannot explain the presence of bromine within the 2D phase. Thus, we presume another formation mechanism exists for the 2D layer, parallel to the 4-FPEAI/PbI_2 reaction.

One of the precursors used to make the 3D perovskite is $PbBr_2$. This precursor could react with 4-FPEAI in the same way PbI_2 does in eq. 1 to form a 2D perovskite containing iodine and bromine, based on this reaction:

$$2(\text{4-FPEAI}) + PbBr_2 \rightarrow (\text{4-FPEA})_2Pb(I_{0.5}Br_{0.5})_4 \qquad \text{Eq. 2}$$

However, the 3D perovskite precursor solution contains less $PbBr_2$ than PbI_2 (1.1mmol of PbI_2 and 0.2mmol of $PbBr_2$). Besides, $PbBr_2$ is more reactive than PbI_2 in forming the 3D perovskite.[47] Hence, there should not be any $PbBr_2$ in the 3D bulk available for reaction with 4-FPEAI. Furthermore, no sign of unreacted $PbBr_2$ is visible in XRD data. Thus, it is likely that when we deposit the 4-FPEAI solution, bromine is already embedded in the crystallized 3D structure and cannot get into the 2D phase by this mechanism.

We speculate that bromine's presence in the 2D layer is induced by a substitution of the 3D perovskite cations (MA, FA, and Cs) by the 2D perovskite spacer cation, here 4-FPEAI, along the following reaction:

$$(Cs,MA,FA)Pb(I_xBr_{1-x})_3 + 2(4\text{-}FPEAI) \rightarrow (4\text{-}FPEA)_2Pb(I_yBr_{1-y})_4 + (I,Br)^- + (Cs,MA,FA)^+ \quad \text{Eq. 3}$$

This mechanism reorganizes the surface to form the 2D perovskite.[54,55] The greater complexation of Pb^{2+} with Br^- than with I^- justifies the greater bromine/iodine ratio in the 2D phase than in the 3D perovskite.[56] Due to the highly polar nature of IPA, it significantly dissolves FA and MA ions.[57] Hence, both organic compounds might be eliminated with excess solvent during the spinning for the 4-FPEAI solution deposition and by the evaporation of the solvent during the 2D layer annealing, explaining their disappearance from XPS measurements on 4-FPEAI treated samples.

To form the n=2 phase $R_2AB_2X_7$ visible in PL measurements, small A-site cations from the 3D perovskite are mandatory. Cs^+ ions are not soluble in IPA, and so they are probably evacuated from the surface less efficiently than FA and MA. However, due to their inorganic nature, they are also less favorable for ionic exchange.[58] For this reason, we explain the predominance of the n=1 phase by the small number of A-site cations available. However, we cannot precisely determine which A-site cation resulting from the reconstruction of the 3D perovskite extreme surface is used to form this n=2 phase, and we assume that all A site cations (FA, MA, and Cs) are involved.

To prove that the 2D layer formation results from a cation exchange mechanism, a new configuration with a lack of PbI_2 in the 3D bulk was considered. A 5mg.mL^{-1} 4-FPEAI solution was deposited on 3D perovskites with two different PbI_2 amounts: -6.2% (a lack of PbI_2) and 2.0% (the excess used for all samples in this study). XRD patterns in Figure 6a show that a similar 2D phase is formed regardless of the PbI_2 excess. For the 2% excess sample, no PbI_2 peak is visible because PbI_2 has been consumed during the reaction with 4-FPEAI. For the -6.2% lack, no PbI_2 peak was observed, consistent with the absence of PbI_2 excess from the composition. In

Supplementary Figure S6, GIXRD on a 3D perovskite with -6.2% PbI_2 and not treated with 4-FPEAI solution confirms this result, showing no PbI_2 peak at the surface of the layer. Hence, if a similar 2D phase is formed without any PbI_2 excess in the 3D bulk, it confirms the presence of a second formation mechanism. PL measurements in Supplementary Figure S7 also confirm that regardless of the PbI_2 excess in the 3D perovskite, a 2D phase is formed. The PL intensities of the 3D phases vary because of the different amounts of PbI_2 affecting the optical properties of the material. Meanwhile, the 2D layer PL intensities are close, indicating a comparable quantity of 2D perovskite formed that does not rely on the PbI_2 excess in the 3D bulk. However, their emission wavelengths slightly differ.

Figure 6b displays the distribution of maximum PL wavelength for the 2D phase regarding the PbI_2 excess in the 4-FPEAI treated 3D perovskites. The 2D phase PL maximum is slightly blue-shifted for the -6.2% PbI_2 lack compared to the 2% excess (508.5 nm versus 510.5 nm). With a lower PbI_2 amount in the layer, the cation exchange mechanism was favored for 2D perovskite formation, leading to a slightly more bromine-rich layer and a blue shift of the PL. An excess of 9.0% was also tested and is presented in Supplementary Figure S8. For this 9% PbI_2 excess, a significant PbI_2 peak is still visible in XRD after 4-FPEAI treatment, as only the PbI_2 excess from the surface and not from the bulk was consumed during the 2D layer formation. For PL, the 2D phase wavelength for the 9% excess is similar to the 2% excess sample, proving that the wavelength shift is not caused by a different composition and bromine/iodine ratio.

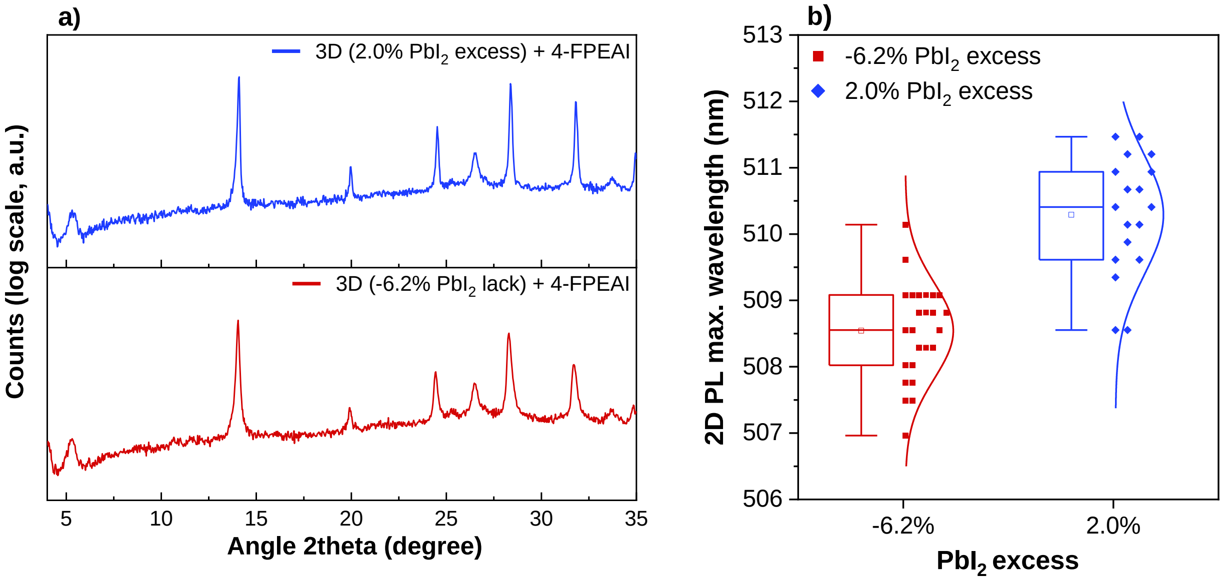

Figure 6. a) Bragg XRD and b) Distribution of 2D phase PL maximum wavelength for 3D perovskites with a -6.2% lack and a 2% excess PbI_2, treated with 5mg.mL^{-1} 4-FPEAI solution.

4. Conclusions

In conclusion, this work shows that the deposition of a 4-FPEAI solution onto a crystallized 3D perovskite forms a few nanometers thick 2D perovskite layer of mostly n=1 phase that can significantly improve the efficiency of solar cell devices. By varying the cation concentration of the deposited solution, we substantially increased the layer thickness up to tens of nanometers. The halide modification in the composition of the 3D perovskite showed us that the bromine inside the 3D phase was also present in the 2D layer, affecting its optical properties. It leads us to conclude that this 2D layer formation results from at least two concomitant mechanisms: the reaction of the 4-FPEAI organic spacer with the excess PbI_2 from the 3D composition and a cation exchange reaction between the 3D phase and 4-FPEAI. We confirmed the presence of this second mechanism by being able to form a 2D perovskite phase even after removing the PbI_2 excess from the 3D perovskite stoichiometry. It also revealed that these mechanisms occur concurrently to form the 2D layer until all the 4-FPEAI cation is consumed, making it the limiting reactant of the process. It emphasizes the importance of the 2D cation concentration in controlling the physical properties of the layer. Because of the cation exchange reaction, the 3D perovskite composition affects the stoichiometry of the 2D layer formed on top, proving the great versatility of 2D perovskites and highlighting new possibilities to tune the composition of this 3D/2D interface. Finally, this work brings new insight into the synthesis mechanisms of these 3D/2D perovskite heterostructures, which could lead to the development of new efficient and functional 3D/2D structures.

Supplementary Information

Illustration of 4-FPEAI treatment, PCE statistics from I-V data, GIXRD patterns, AFM topographic images, statistics on Sq and Sa roughness measured with AFM and optical microscopy, PL spectra, and statistics on maximum wavelength distribution from PL data.

Acknowledgments

This project has been supported by the French Government in the frame of the investment program for the future (Programme d'Investissement d'Avenir - ANR-IEED-002-01).
The work of Thomas Campos is supported by the labeX Charmmmat (University Paris-Saclay).
This work has also been financially supported by the French National Research Agency (ANR HYPERSOL), contract ANR-18-CE05-0021.

TOC Graphic

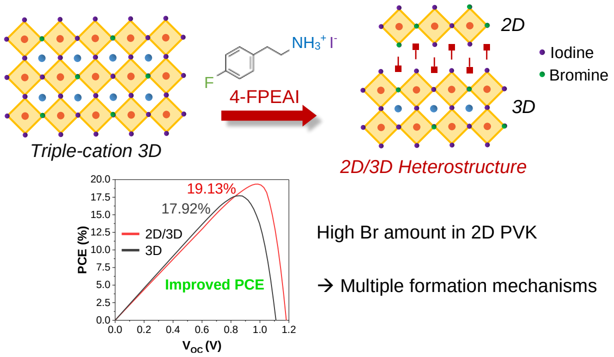

High Br amount in 2D PVK

→ Multiple formation mechanisms

References

(1) *Best Research-Cell Efficiency Chart | Photovoltaic Research | NREL*. https://www.nrel.gov/pv/cell-efficiency.html (accessed 2022-04-08).

(2) Green, M. A.; Dunlop, E. D.; Hohl-Ebinger, J.; Yoshita, M.; Kopidakis, N.; Hao, X. Solar Cell Efficiency Tables (Version 59). *Prog. Photovolt. Res. Appl.* **2022**, *30* (1), 3–12. https://doi.org/10.1002/pip.3506.

(3) Kojima, A.; Teshima, K.; Shirai, Y.; Miyasaka, T. Organometal Halide Perovskites as Visible-Light Sensitizers for Photovoltaic Cells. *J. Am. Chem. Soc.* **2009**, *131* (17), 6050–6051. https://doi.org/10.1021/ja809598r.

(4) Kim, H.-S.; Lee, C.-R.; Im, J.-H.; Lee, K.-B.; Moehl, T.; Marchioro, A.; Moon, S.-J.; Humphry-Baker, R.; Yum, J.-H.; Moser, J. E.; et al. Lead Iodide Perovskite Sensitized All-Solid-State Submicron Thin Film Mesoscopic Solar Cell with Efficiency Exceeding 9%. *Sci. Rep.* **2012**, *2* (1), 591. https://doi.org/10.1038/srep00591.

(5) Min, H.; Lee, D. Y.; Kim, J.; Kim, G.; Lee, K. S.; Kim, J.; Paik, M. J.; Kim, Y. K.; Kim, K. S.; Kim, M. G.; et al. Perovskite Solar Cells with Atomically Coherent Interlayers on SnO2 Electrodes. *Nature* **2021**, *598* (7881), 444–450. https://doi.org/10.1038/s41586-021-03964-8.

(6) Chien Sum, T.; Mathews, N. Advancements in Perovskite Solar Cells: Photophysics behind the Photovoltaics. *Energy Environ. Sci.* **2014**, *7* (8), 2518–2534. https://doi.org/10.1039/C4EE00673A.

(7) Zhumekenov, A. A.; Saidaminov, M. I.; Haque, M. A.; Alarousu, E.; Sarmah, S. P.; Murali, B.; Dursun, I.; Miao, X.-H.; Abdelhady, A. L.; Wu, T.; et al. Formamidinium Lead Halide Perovskite Crystals with Unprecedented Long Carrier Dynamics and Diffusion Length. *ACS Energy Lett.* **2016**, *1* (1), 32–37. https://doi.org/10.1021/acsenergylett.6b00002.

(8) Johnston, M. B.; Herz, L. M. Hybrid Perovskites for Photovoltaics: Charge-Carrier Recombination, Diffusion, and Radiative Efficiencies. *Acc. Chem. Res.* **2016**, *49* (1), 146–154. https://doi.org/10.1021/acs.accounts.5b00411.

(9) Kim, H.-S.; Mora-Sero, I.; Gonzalez-Pedro, V.; Fabregat-Santiago, F.; Juarez-Perez, E. J.; Park, N.-G.; Bisquert, J. Mechanism of Carrier Accumulation in Perovskite Thin-Absorber Solar Cells. *Nat. Commun.* **2013**, *4* (1), 2242. https://doi.org/10.1038/ncomms3242.

(10) Werner, J.; Niesen, B.; Ballif, C. Perovskite/Silicon Tandem Solar Cells: Marriage of Convenience or True Love Story? – An Overview. *Adv. Mater. Interfaces* **2018**, *5* (1), 1700731. https://doi.org/10.1002/admi.201700731.

(11) Yu, Z. (Jason); Leilaeioun, M.; Holman, Z. Selecting Tandem Partners for Silicon Solar Cells. *Nat. Energy* **2016**, *1* (11), 1–4. https://doi.org/10.1038/nenergy.2016.137.

(12) Wang, R.; Mujahid, M.; Duan, Y.; Wang, Z.-K.; Xue, J.; Yang, Y. A Review of Perovskites Solar Cell Stability. *Adv. Funct. Mater.* **2019**, *29* (47), 1808843. https://doi.org/10.1002/adfm.201808843.

(13) K. Rao, M.; Sangeetha, D. N.; Selvakumar, M.; Sudhakar, Y. N.; Mahesha, M. G. Review on Persistent Challenges of Perovskite Solar Cells' Stability. *Sol. Energy* **2021**, *218*, 469–491. https://doi.org/10.1016/j.solener.2021.03.005.

(14) Cheng, Y.; Ding, L. Pushing Commercialization of Perovskite Solar Cells by Improving Their Intrinsic Stability. *Energy Environ. Sci.* **2021**, *14* (6), 3233–3255. https://doi.org/10.1039/D1EE00493J.

(15) Jeong, J.; Kim, M.; Seo, J.; Lu, H.; Ahlawat, P.; Mishra, A.; Yang, Y.; Hope, M. A.; Eickemeyer, F. T.; Kim, M.; et al. Pseudo-Halide Anion Engineering for α-FAPbI 3 Perovskite Solar Cells. *Nature* **2021**, *592* (7854), 381–385. https://doi.org/10.1038/s41586-021-03406-5.

(16) Bu, T.; Liu, X.; Zhou, Y.; Yi, J.; Huang, X.; Luo, L.; Xiao, J.; Ku, Z.; Peng, Y.; Huang, F.; et al. A Novel Quadruple-Cation Absorber for Universal Hysteresis Elimination for High Efficiency and Stable Perovskite Solar Cells. *Energy Environ. Sci.* **2017**, *10* (12), 2509–2515. https://doi.org/10.1039/C7EE02634J.

(17) Grancini, G.; Roldán-Carmona, C.; Zimmermann, I.; Mosconi, E.; Lee, X.; Martineau, D.; Narbey, S.; Oswald, F.; De Angelis, F.; Graetzel, M.; et al. One-Year Stable Perovskite Solar Cells by 2D/3D Interface Engineering. *Nat. Commun.* **2017**, *8*, 15684. https://doi.org/10.1038/ncomms15684.

(18) Noh, M. F. M.; Teh, C. H.; Daik, R.; Lim, E. L.; Yap, C. C.; Ibrahim, M. A.; Ludin, N. A.; Yusoff, A. R. bin M.; Jang, J.; Teridi, M. A. M. The Architecture of the Electron Transport Layer for a Perovskite Solar Cell. *J. Mater. Chem. C* **2018**, *6* (4), 682–712. https://doi.org/10.1039/C7TC04649A.

(19) Arora, N.; Dar, M. I.; Hinderhofer, A.; Pellet, N.; Schreiber, F.; Zakeeruddin, S. M.; Grätzel, M. Perovskite Solar Cells with CuSCN Hole Extraction Layers Yield Stabilized Efficiencies Greater than 20%. *Science* **2017**, *358* (6364), 768–771. https://doi.org/10.1126/science.aam5655.

(20) Singh, A. N.; Kajal, S.; Kim, J.; Jana, A.; Kim, J. Y.; Kim, K. S. Interface Engineering Driven Stabilization of Halide Perovskites against Moisture, Heat, and Light for Optoelectronic Applications. *Adv. Energy Mater.* **2020**, *10* (30), 2000768. https://doi.org/10.1002/aenm.202000768.

(21) Fairfield, D. J.; Sai, H.; Narayanan, A.; Passarelli, J. V.; Chen, M.; Palasz, J.; Palmer, L. C.; Wasielewski, M. R.; Stupp, S. I. Structure and Chemical Stability in Perovskite–Polymer Hybrid Photovoltaic Materials. *J. Mater. Chem. A* **2019**, *7* (4), 1687–1699. https://doi.org/10.1039/C8TA07545J.

(22) Guo, P.; Ye, Q.; Yang, X.; Zhang, J.; Xu, F.; Shchukin, D.; Wei, B.; Wang, H. Surface & Grain Boundary Co-Passivation by Fluorocarbon Based Bifunctional Molecules for Perovskite Solar Cells with Efficiency over 21%. *J. Mater. Chem. A* **2019**, *7* (6), 2497–2506. https://doi.org/10.1039/C8TA11524A.

(23) Yan, J.; Qiu, W.; Wu, G.; Heremans, P.; Chen, H. Recent Progress in 2D/Quasi-2D Layered Metal Halide Perovskites for Solar Cells. *J. Mater. Chem. A* **2018**, *6* (24), 11063–11077. https://doi.org/10.1039/C8TA02288G.

(24) Hu, Y.; Schlipf, J.; Wussler, M.; Petrus, M. L.; Jaegermann, W.; Bein, T.; Müller-Buschbaum, P.; Docampo, P. Hybrid Perovskite/Perovskite Heterojunction Solar Cells. *ACS Nano* **2016**, *10* (6), 5999–6007. https://doi.org/10.1021/acsnano.6b01535.

(25) Mahmud, M. A.; Duong, T.; Peng, J.; Wu, Y.; Shen, H.; Walter, D.; Nguyen, H. T.; Mozaffari, N.; Tabi, G. D.; Catchpole, K. R.; et al. Origin of Efficiency and Stability Enhancement in High-Performing Mixed Dimensional 2D-3D Perovskite Solar Cells: A Review. *Adv. Funct. Mater.* **2022**, *32* (3), 2009164. https://doi.org/10.1002/adfm.202009164.

(26) Zhang, Y.; Park, N.-G. Quasi-Two-Dimensional Perovskite Solar Cells with Efficiency Exceeding 22%. *ACS Energy Lett.* **2022**, *7* (2), 757–765. https://doi.org/10.1021/acsenergylett.1c02645.

(27) Mao, L.; Stoumpos, C. C.; Kanatzidis, M. G. Two-Dimensional Hybrid Halide Perovskites: Principles and Promises. *J. Am. Chem. Soc.* **2019**, *141* (3), 1171–1190. https://doi.org/10.1021/jacs.8b10851.

(28) Chen, Y.; Sun, Y.; Peng, J.; Tang, J.; Zheng, K.; Liang, Z. 2D Ruddlesden–Popper Perovskites for Optoelectronics. *Adv. Mater.* **2018**, *30* (2), 1703487. https://doi.org/10.1002/adma.201703487.

(29) Fu, W.; Chen, H.; Jen, A. K.-Y. Two-Dimensional Perovskites for Photovoltaics. *Mater. Today Nano* **2021**, *14*, 100117. https://doi.org/10.1016/j.mtnano.2021.100117.

(30) Di, J.; Chang, J.; Liu, S. (Frank). Recent Progress of Two-Dimensional Lead Halide Perovskite Single Crystals: Crystal Growth, Physical Properties, and Device Applications. *EcoMat* **2020**, *2* (3), e12036. https://doi.org/10.1002/eom2.12036.

(31) de Holanda, M. S.; Szostak, R.; Marchezi, P. E.; Duarte, L. G. T. A.; Germino, J. C.; Atvars, T. D. Z.; Nogueira, A. F. In Situ 2D Perovskite Formation and the Impact of the 2D/3D Structures on Performance and Stability of Perovskite Solar Cells. *Sol. RRL* **2019**, *3* (9), 1900199. https://doi.org/10.1002/solr.201900199.

(32) Alanazi, A. Q.; Almalki, M. H.; Mishra, A.; Kubicki, D. J.; Wang, Z.; Merten, L.; Eickemeyer, F. T.; Zhang, H.; Ren, D.; Alyamani, A. Y.; et al. Benzylammonium-Mediated Formamidinium Lead Iodide Perovskite Phase Stabilization for Photovoltaics. *Adv. Funct. Mater.* **2021**, *31* (30), 2101163. https://doi.org/10.1002/adfm.202101163.

(33) Kim, D.; Jung, H. J.; Park, I. J.; Larson, B. W.; Dunfield, S. P.; Xiao, C.; Kim, J.; Tong, J.; Boonmongkolras, P.; Ji, S. G.; et al. Efficient, Stable Silicon Tandem Cells Enabled by Anion-Engineered Wide-Bandgap Perovskites. *Science* **2020**, *368* (6487), 155–160. https://doi.org/10.1126/science.aba3433.

(34) Li, J.; Wu, M.; Yang, G.; Zhang, D.; Wang, Z.; Zheng, D.; Yu, J. Bottom-up Passivation Effects by Using 3D/2D Mix Structure for High Performance p-i-n Perovskite Solar Cells. *Sol. Energy* **2020**, *205*, 44–50. https://doi.org/10.1016/j.solener.2020.05.042.

(35) Wei, Y.; Audebert, P.; Galmiche, L.; Lauret, J.-S.; Deleporte, E. Synthesis, Optical Properties and Photostability of Novel Fluorinated Organic–Inorganic Hybrid (R –NH_3)$_2$ PbX_4 Semiconductors. *J. Phys. Appl. Phys.* **2013**, *46* (13), 135105. https://doi.org/10.1088/0022-3727/46/13/135105.

(36) Gharibzadeh, S.; Nejand, B. A.; Jakoby, M.; Abzieher, T.; Hauschild, D.; Moghadamzadeh, S.; Schwenzer, J. A.; Brenner, P.; Schmager, R.; Haghighirad, A. A.; et al. Record Open-Circuit Voltage Wide-Bandgap Perovskite Solar Cells Utilizing 2D/3D Perovskite Heterostructure. *Adv. Energy Mater.* **2019**, *0* (0), 1803699. https://doi.org/10.1002/aenm.201803699.

(37) Degani, M.; An, Q.; Albaladejo-Siguan, M.; Hofstetter, Y. J.; Cho, C.; Paulus, F.; Grancini, G.; Vaynzof, Y. 23.7% Efficient Inverted Perovskite Solar Cells by Dual Interfacial Modification. *Sci. Adv. 7* (49), eabj7930. https://doi.org/10.1126/sciadv.abj7930.

(38) Kim, E.-B.; Akhtar, M. S.; Shin, H.-S.; Ameen, S.; Nazeeruddin, M. K. A Review on Two-Dimensional (2D) and 2D-3D Multidimensional Perovskite Solar Cells: Perovskites Structures, Stability, and Photovoltaic Performances. *J. Photochem. Photobiol. C Photochem. Rev.* **2021**, *48*, 100405. https://doi.org/10.1016/j.jphotochemrev.2021.100405.

(39) Mahmud, M. A.; Duong, T.; Yin, Y.; Pham, H. T.; Walter, D.; Peng, J.; Wu, Y.; Li, L.; Shen, H.; Wu, N.; et al. Double-Sided Surface Passivation of 3D Perovskite Film for High-Efficiency Mixed-Dimensional Perovskite Solar Cells. *Adv. Funct. Mater.* **2020**, *30* (7), 1907962. https://doi.org/10.1002/adfm.201907962.

(40) Sutanto, A. A.; Szostak, R.; Drigo, N.; Queloz, V. I. E.; Marchezi, P. E.; Germino, J. C.; Tolentino, H. C. N.; Nazeeruddin, M. K.; Nogueira, A. F.; Grancini, G. In Situ Analysis Reveals the Role of 2D Perovskite in Preventing Thermal-Induced Degradation in 2D/3D Perovskite Interfaces. *Nano Lett.* **2020**. https://doi.org/10.1021/acs.nanolett.0c01271.

(41) Bouduban, M. E. F.; Queloz, V. I. E.; Caselli, V. M.; Cho, K. T.; Paek, S.; Roldan-Carmona, C.; Richter, L. J.; Moser, J. E.; Savenije, T. J.; Nazeeruddin, M. K.; et al. Crystal Orientation Drives the Interface Physics at Two/Three-Dimensional Hybrid Perovskites. *J. Phys. Chem. Lett.* **2019**, *10* (19), 5713–5720. https://doi.org/10.1021/acs.jpclett.9b02224.

(42) Caprioglio, P.; Cruz, D. S.; Caicedo-Dávila, S.; Zu, F.; Sutanto, A. A.; Peña-Camargo, F.; Kegelmann, L.; Meggiolaro, D.; Gregori, L.; Wolff, C. M.; et al. Bi-Functional Interfaces by Poly(Ionic Liquid) Treatment in Efficient Pin and Nip Perovskite Solar Cells. *Energy Environ. Sci.* **2021**, *14* (8), 4508–4522. https://doi.org/10.1039/D1EE00869B.

(43) Sutanto, A. A.; Drigo, N.; Queloz, V. I. E.; Garcia-Benito, I.; Kirmani, A. R.; Richter, L. J.; Schouwink, P. A.; Cho, K. T.; Paek, S.; Nazeeruddin, M. K.; et al. Dynamical Evolution of the 2D/3D Interface: A Hidden Driver behind Perovskite Solar Cell Instability. *J. Mater. Chem. A* **2020**, *8* (5), 2343–2348. https://doi.org/10.1039/C9TA12489F.

(44) Zhou, Q.; Liang, L.; Hu, J.; Cao, B.; Yang, L.; Wu, T.; Li, X.; Zhang, B.; Gao, P. High-Performance Perovskite Solar Cells with Enhanced Environmental Stability Based on a (p-FC6H4C2H4NH3)2[PbI4] Capping Layer. *Adv. Energy Mater.* **2019**, *0* (0), 1802595. https://doi.org/10.1002/aenm.201802595.

(45) Qiu, Y.; Liang, J.; Zhang, Z.; Deng, Z.; Xu, H.; He, M.; Wang, J.; Yang, Y.; Kong, L.; Chen, C.-C. Tuning the Interfacial Dipole Moment of Spacer Cations for Charge Extraction in Efficient and Ultrastable Perovskite Solar Cells. *J. Phys. Chem. C* **2021**, *125* (2), 1256–1268. https://doi.org/10.1021/acs.jpcc.0c09606.

(46) Cacovich, S.; Messou, D.; Bercegol, A.; Béchu, S.; Yaiche, A.; Shafique, H.; Rousset, J.; Schulz, P.; Bouttemy, M.; Lombez, L. Light-Induced Passivation in Triple Cation Mixed Halide Perovskites: Interplay between Transport Properties and Surface Chemistry. *ACS Appl. Mater. Interfaces* **2020**, *12* (31), 34784–34794. https://doi.org/10.1021/acsami.0c06844.

(47) Jesper Jacobsson, T.; Correa-Baena, J.-P.; Pazoki, M.; Saliba, M.; Schenk, K.; Grätzel, M.; Hagfeldt, A. Exploration of the Compositional Space for Mixed Lead Halogen Perovskites for High Efficiency Solar Cells. *Energy Environ. Sci.* **2016**, *9* (5), 1706–1724. https://doi.org/10.1039/C6EE00030D.

(48) Liu, Y.; Akin, S.; Pan, L.; Uchida, R.; Arora, N.; Milić, J. V.; Hinderhofer, A.; Schreiber, F.; Uhl, A. R.; Zakeeruddin, S. M.; et al. Ultrahydrophobic 3D/2D Fluoroarene Bilayer-Based Water-Resistant Perovskite Solar Cells with Efficiencies Exceeding 22%. *Sci. Adv.* **2019**, *5* (6), eaaw2543. https://doi.org/10.1126/sciadv.aaw2543.

(49) Delport, G.; Chehade, G.; Lédée, F.; Diab, H.; Milesi-Brault, C.; Trippé-Allard, G.; Even, J.; Lauret, J.-S.; Deleporte, E.; Garrot, D. Exciton–Exciton Annihilation in Two-Dimensional Halide Perovskites at Room Temperature. *J. Phys. Chem. Lett.* **2019**, *10* (17), 5153–5159. https://doi.org/10.1021/acs.jpclett.9b01595.

(50) Protesescu, L.; Yakunin, S.; Bodnarchuk, M. I.; Krieg, F.; Caputo, R.; Hendon, C. H.; Yang, R. X.; Walsh, A.; Kovalenko, M. V. Nanocrystals of Cesium Lead Halide Perovskites (CsPbX3, X = Cl, Br, and I): Novel Optoelectronic Materials Showing Bright Emission with Wide Color Gamut. *Nano Lett.* **2015**, *15* (6), 3692–3696. https://doi.org/10.1021/nl5048779.

(51) Lanty, G.; Jemli, K.; Wei, Y.; Leymarie, J.; Even, J.; Lauret, J.-S.; Deleporte, E. Room-Temperature Optical Tunability and Inhomogeneous Broadening in 2D-Layered Organic–Inorganic Perovskite Pseudobinary Alloys. *J. Phys. Chem. Lett.* **2014**, *5* (22), 3958–3963. https://doi.org/10.1021/jz502086e.

(52) Yaffe, O.; Chernikov, A.; Norman, Z. M.; Zhong, Y.; Velauthapillai, A.; van der Zande, A.; Owen, J. S.; Heinz, T. F. Excitons in Ultrathin Organic-Inorganic Perovskite Crystals. *Phys. Rev. B* **2015**, *92* (4), 045414. https://doi.org/10.1103/PhysRevB.92.045414.

(53) Blancon, J.-C.; Stier, A. V.; Tsai, H.; Nie, W.; Stoumpos, C. C.; Traoré, B.; Pedesseau, L.; Kepenekian, M.; Katsutani, F.; Noe, G. T.; et al. Scaling Law for Excitons in 2D Perovskite Quantum Wells. *Nat. Commun.* **2018**, *9* (1), 2254. https://doi.org/10.1038/s41467-018-04659-x.

(54) Huang, W.; Sadhu, S.; Sapkota, P.; Ptasinska, S. In Situ Identification of Cation-Exchange-Induced Reversible Transformations of 3D and 2D Perovskites. *Chem. Commun.* **2018**, *54* (46), 5879–5882. https://doi.org/10.1039/C8CC02801J.

(55) Tan, S.; Huang, T.; Yavuz, I.; Wang, R.; Weber, M. H.; Zhao, Y.; Abdelsamie, M.; Liao, M. E.; Wang, H.-C.; Huynh, K.; et al. Surface Reconstruction of Halide Perovskites During Post-Treatment. *J. Am. Chem. Soc.* **2021**. https://doi.org/10.1021/jacs.1c00757.

(56) Yoon, S. J.; Stamplecoskie, K. G.; Kamat, P. V. How Lead Halide Complex Chemistry Dictates the Composition of Mixed Halide Perovskites. *J. Phys. Chem. Lett.* **2016**, *7* (7), 1368–1373. https://doi.org/10.1021/acs.jpclett.6b00433.

(57) Yoo, J. J.; Wieghold, S.; Sponseller, M. C.; Chua, M. R.; Bertram, S. N.; Hartono, N. T. P.; Tresback, J. S.; Hansen, E. C.; Correa-Baena, J.-P.; Bulović, V.; et al. An Interface Stabilized Perovskite Solar Cell with High Stabilized Efficiency and Low Voltage Loss. *Energy Environ. Sci.* **2019**, *12* (7), 2192–2199. https://doi.org/10.1039/C9EE00751B.

(58) Liu, T.; Zhang, J.; Qin, M.; Wu, X.; Li, F.; Lu, X.; Zhu, Z.; Jen, A. K.-Y. Modifying Surface Termination of CsPbI3 Grain Boundaries by 2D Perovskite Layer for Efficient and Stable Photovoltaics. *Adv. Funct. Mater.* **2021**, *31* (15), 2009515. https://doi.org/10.1002/adfm.202009515.

SUPPORTING INFORMATION

Unraveling the Formation Mechanism of 2D/3D Perovskite Heterostructure for Perovskite Solar Cells using Multi-Method haracterization

Thomas Campos *,[1,2], *Pia Dally* [2,5], *Stéphanie Gbegnon* [2], *Alexandre Blaizot* [2], *Gaëlle Trippé-Allard* [1], *Marion Provost* [2], *Muriel Bouttemy* [5], *Aurélien Duchatelet* [2,3], *Damien Garrot* [4], *Jean Rousset* [2,3], *Emmanuelle Deleporte* [1]

[1] Lumière, Matière et Interfaces (LuMIn) Laboratory, Université Paris-Saclay, ENS Paris-Saclay, CNRS, CentraleSupelec, 91190 Gif-sur-Yvette, France * thomas.campos@ens-paris-saclay.fr

[2] Institut Photovoltaïque d'Ile-de-France (IPVF), 18 Boulevard Thomas Gobert, 91120 Palaiseau, France

[3] EDF R&D, Boulevard Gaspard Monge, 91120 Palaiseau, France

[4] Groupe d'Etudes de la Matière Condensée (GEMAC), Université Versailles Saint-Quentin en Yvelines, CNRS, 45 avenue des Etats-Unis, 78000 Versailles, France

[5] Institut Lavoisier de Versailles (ILV), Université de Versailles Saint-Quentin-en-Yvelines, Université Paris-Saclay, CNRS, UMR 8180, 45 avenue des États-Unis, 78035 Versailles, France

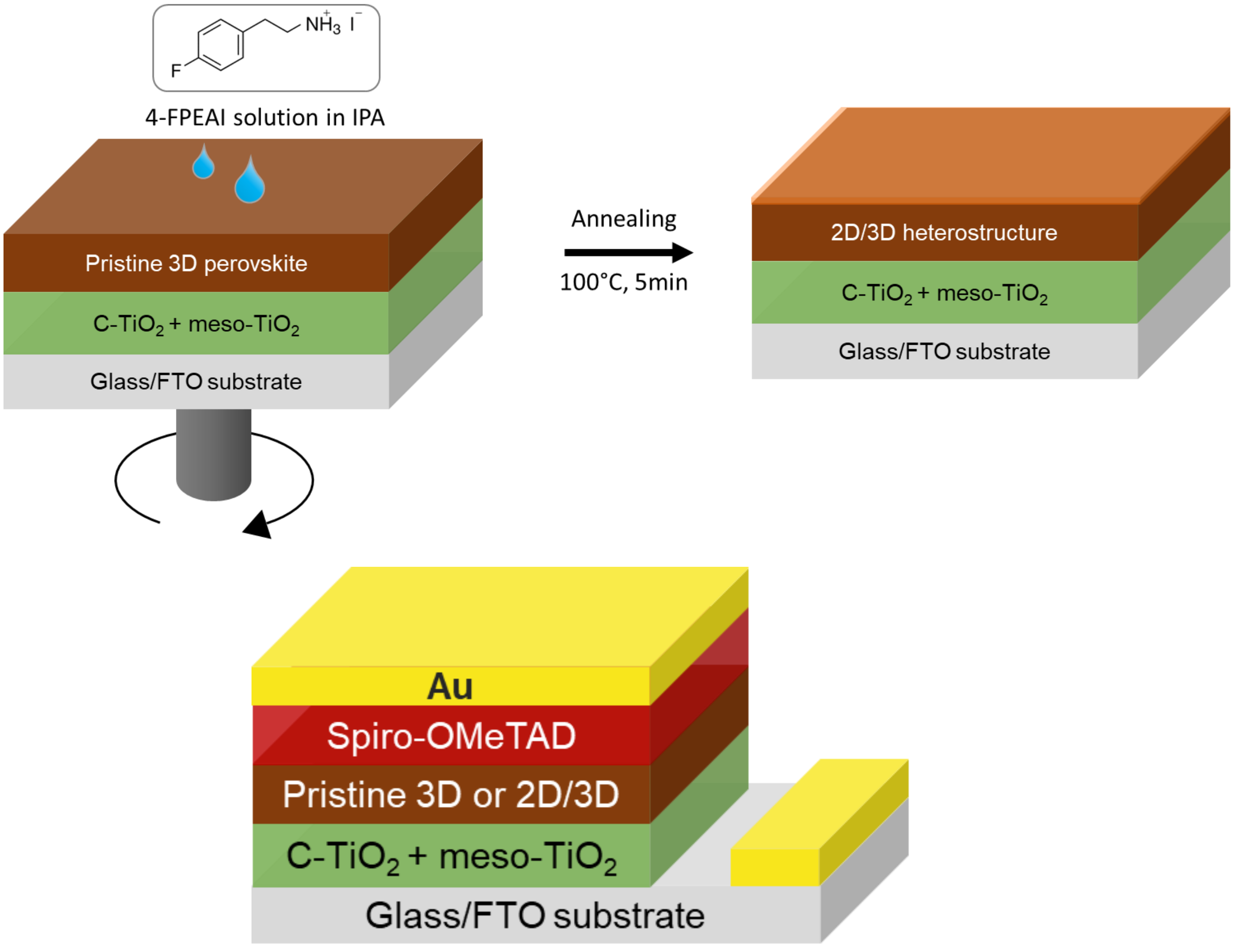

Supplementary Figure S1. Illustration of the 4-FPEAI treatment process on a 3D perovskite, and NIP architecture of the solar cell devices.

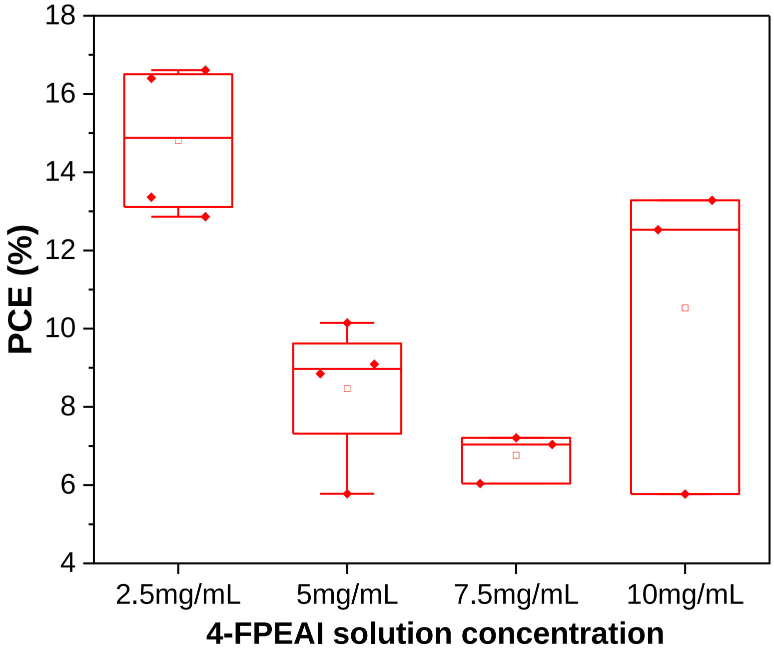

Supplementary Figure S2. PCE comparison between several concentrations for 4-FPEAI treatment.

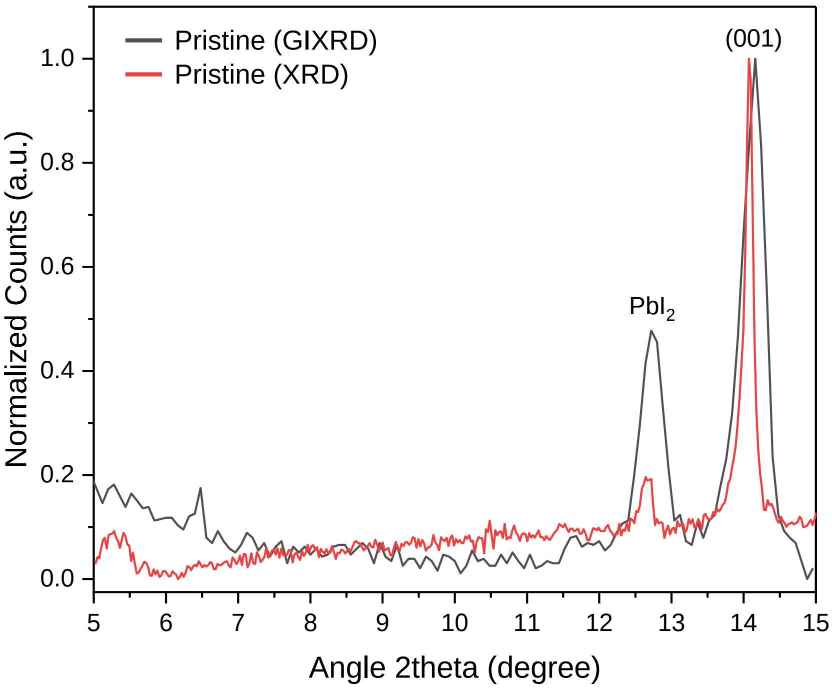

Supplementary Figure S3. Bragg-Brentano XRD and grazing-incidence XRD patterns of a pristine 3D perovskite.

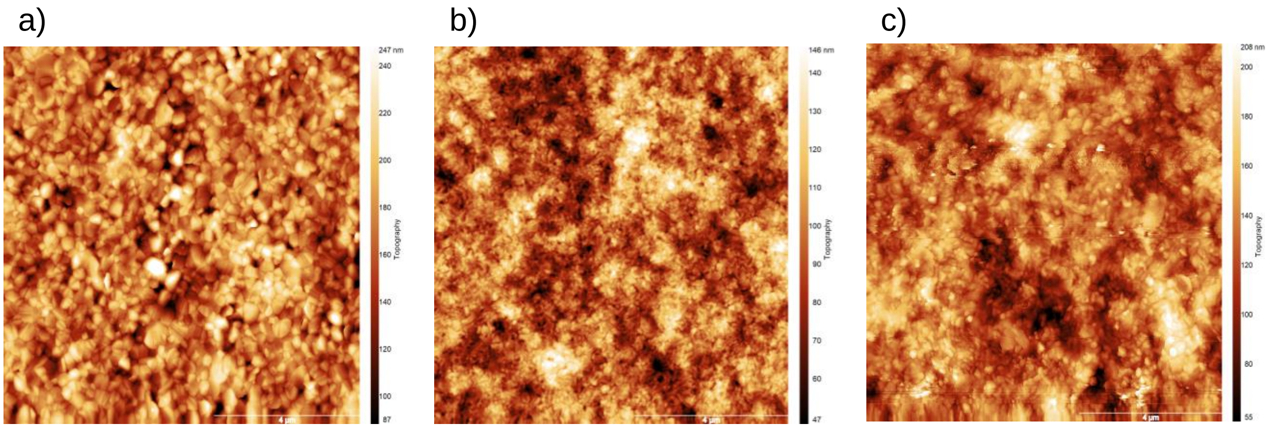

Supplementary Figure S4. AFM topographic scans of a) pristine, b) 2.5mg.mL^{-1}, and c) 10mg.mL^{-1} samples.

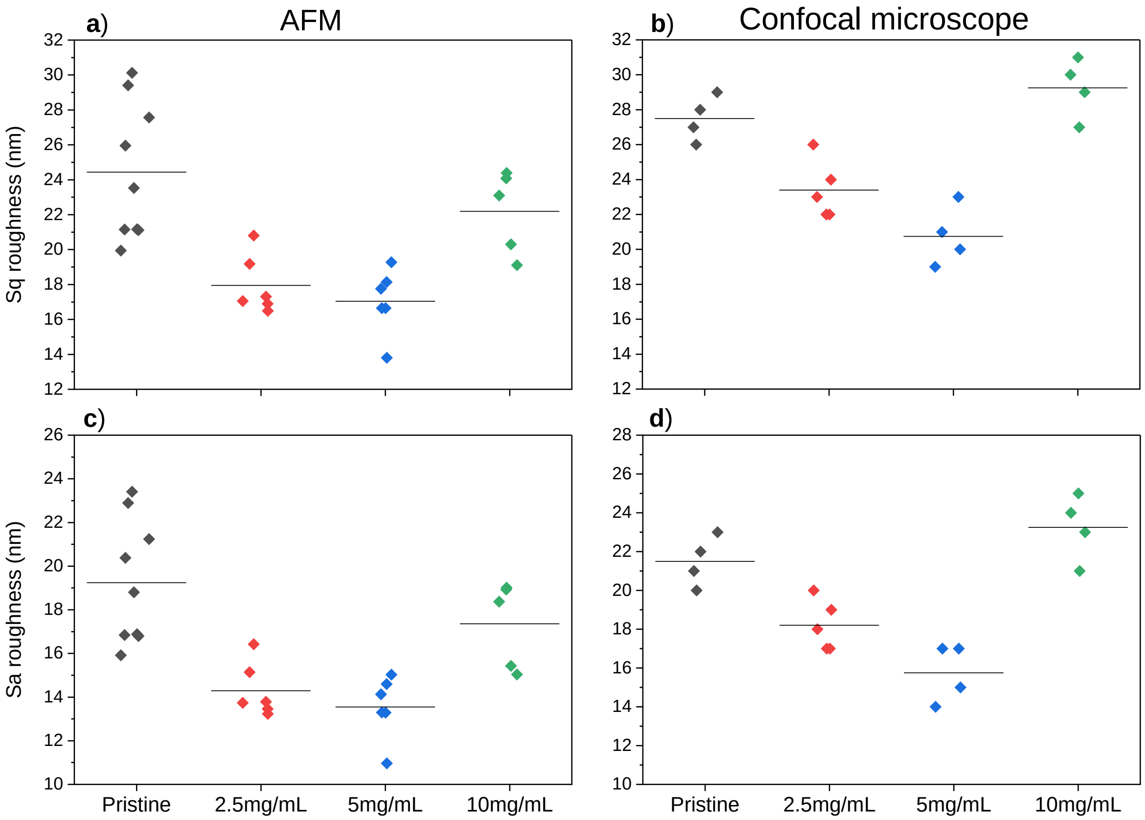

Supplementary Figure S5. Distribution of Sq and Sa roughness values for measurements with a), c) an atomic force microscope or with b), d) a confocal microscope, for pristine and 4-FPEAI treated samples for all concentration (2.5, 5, and 10mg.mL^{-1}).

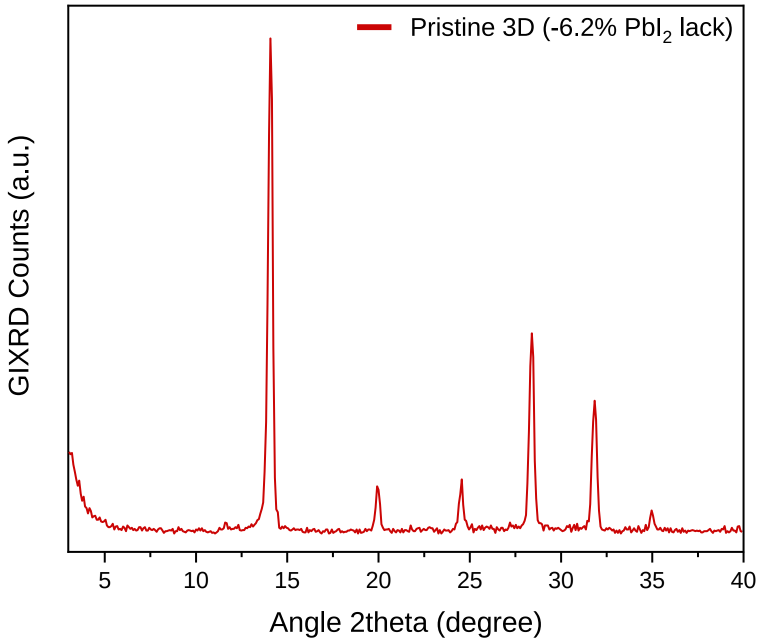

Supplementary Figure S6. GIXRD diffractogram of an untreated 3D perovskite with a -6.2% PbI2 lack.

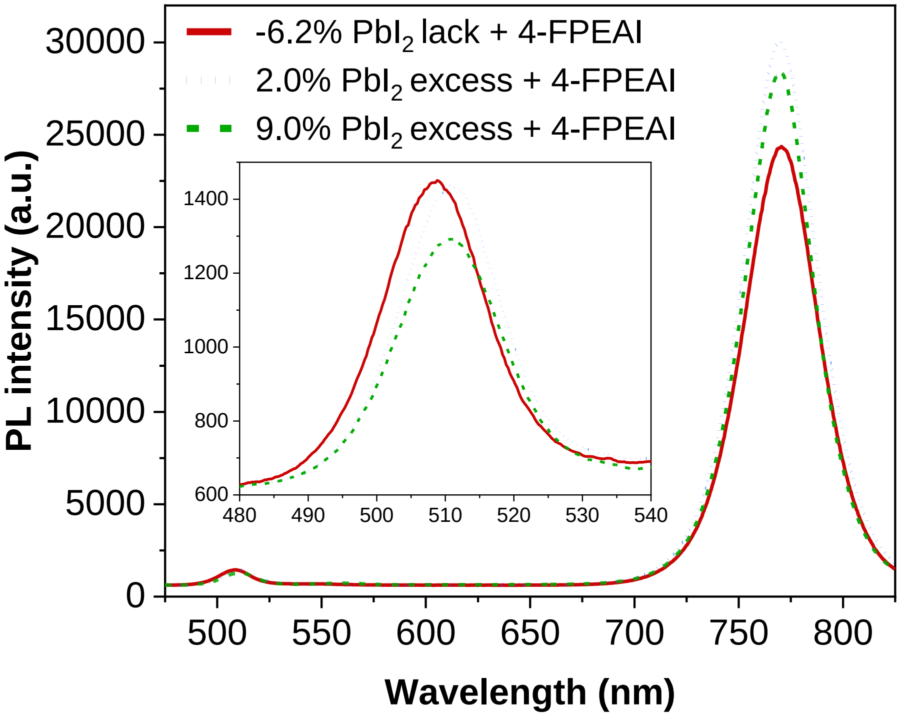

Supplementary Figure S7. PL spectra of 4-FPEAI treated 3D perovskites containing -6.2%, 2%, or 9% PbI_2 excess.

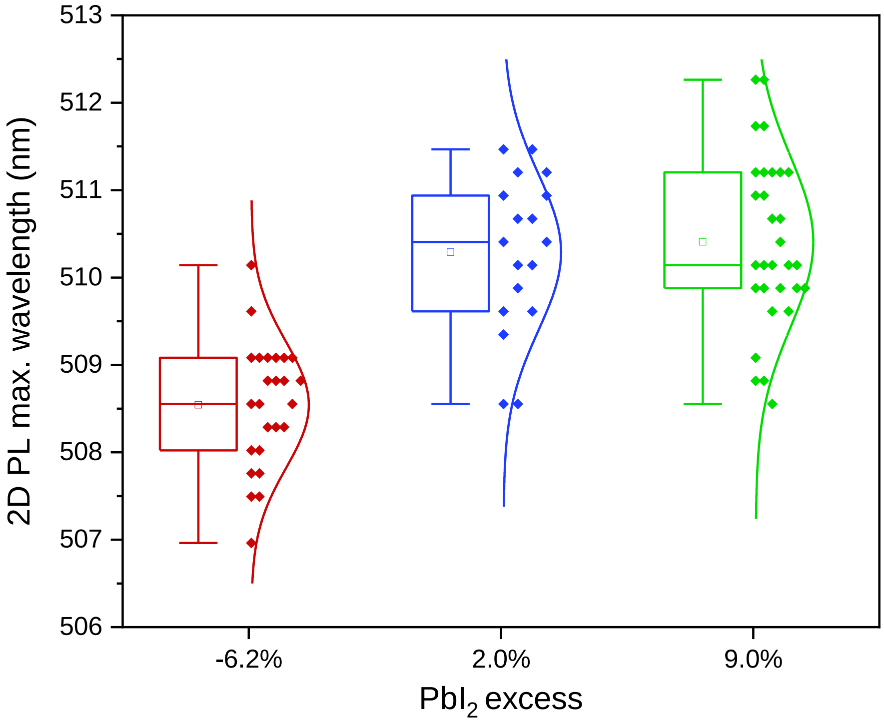

Supplementary Figure S8. Statistical distribution of 2D phase maximum PL wavelength for -6.2%, 2%, or 9% PbI2 excess in the 3D composition.